

# Probing Vibrational Strong Coupling of Molecules with Wavelength-Modulated Raman Spectroscopy

Kishan S. Menghrajani,\* Mingzhou Chen, Kishan Dholakia, and William L. Barnes\*

Raman spectroscopy is a powerful technique that enables fingerprinting of materials, molecules, and chemical environments by probing vibrational resonances. In many applications, the desired Raman signals are masked by fluorescence, either from the molecular system being studied, or from adjacent metallic nanostructures. Here, it is shown that wavelength-modulated Raman spectroscopy provides a powerful way to significantly reduce the strength of the fluorescence background, thereby allowing the desired Raman signals to be clearly recorded. This approach is made use of to explore Raman scattering in the context of vibrational strong coupling, an area that has thus far been problematic to visualise. Specifically, strong coupling between the vibrational modes in a polymer and two types of confined light field, the fundamental mode of a metal-clad microcavity, and the surface-plasmon modes of an adjacent thin metal film are looked at. While clear advantages in using the wavelength-modulated Raman approach are found, these results on strong coupling are inconclusive, and highlight the need for more work in this exciting topic area.

that are shifted from that of the incident laser light. In particular, peaks appear in the spectrum of the scattered light that correspond to vibrational resonances of the molecules/materials of which the sample is composed. These spectral peaks form the characteristic fingerprints of the molecules/materials under investigation; the study of such spectra is known as Raman spectroscopy and has become a well-established and powerful analytic technique.<sup>[5]</sup> Unfortunately, Raman signals are very weak with cross-sections of order  $10^{-30}$  cm<sup>2</sup> for non-resonant Raman and  $10^{-24}$  cm<sup>2</sup> for resonant Raman.<sup>[6]</sup> In many situations, these very weak signals are swamped by light produced by other processes, notably fluorescence, which can be many orders of magnitude stronger than the Raman signal. Background fluorescence is particularly problematic when the

samples to be investigated are dyes/pigments,<sup>[3]</sup> for example, resonant Raman,<sup>[6]</sup> and also when they involve metals.<sup>[7]</sup> In both cases, fluorescence can be so significant as to mask the desired Raman signals.

Various approaches have been adopted to try and deal with the background problem,<sup>[8,9]</sup> and they fall into three broad categories. First, post-processing can be used to try and subtract the background.<sup>[10,11]</sup> Although appealing and commonly used, this approach has its drawbacks, especially in that it does not overcome the problem of noise in the background signal. Second, one can move to the time-domain. Raman scattering is an instantaneous process, whereas fluorescence occurs over a protracted time-scale; however, this approach comes at a very significant increase in complexity.<sup>[12]</sup> Third, a differential approach can be adopted. Here, the idea is to modify the way the data are acquired so as to directly filter out the background and its associated noise. A number of such approaches have been successfully deployed. One technique is based on acquiring spectra for slightly different grating settings in the spectrometer.<sup>[7]</sup> Another approach is to subtract two Raman spectra obtained with different polarization configurations.<sup>[13]</sup> Then, there are techniques that make use of the fact that if the pump wavelength is shifted the Raman peaks will also move in wavelength, but the fluorescence will not. Spectra acquired at two or more closely spaced pump wavelengths can thus be processed to provide a differential signal that largely eliminates the background;<sup>[14]</sup> this technique is known as shifted excitation Raman difference spectroscopy (SERDS). We make use of one variant of this approach here, that of wavelength-modulated Raman spectroscopy (WMRS). WMRS<sup>[15]</sup> is a significant improvement on

## 1. Introduction

Raman spectroscopy has evolved into a powerful technique that is exploited in many areas of science, engineering, the arts, and the humanities. Recent examples include the use of Raman spectroscopy to identify the composition of atomic layer Van der Waals materials,<sup>[1,2]</sup> provide a tool in the diagnosis of disease,<sup>[3]</sup> and assist in the conservation and analysis of medieval pigments and manuscripts.<sup>[4]</sup> When a sample is illuminated by a monochromatic light source, for example, a laser, most of the scattered light has the same frequency (wavelength) as the laser; that is, it has been elastically scattered. However, a very small fraction of the scattered light emerges at wavelengths

K. S. Menghrajani, W. L. Barnes  
University of Exeter - Department of Physics and Astronomy  
University of Exeter  
Exeter EX4 4QL, UK  
E-mail: k.s.menghrajani@exeter.ac.uk; w.l.barnes@exeter.ac.uk  
M. Chen, K. Dholakia  
SUPA  
School of Physics and Astronomy  
University of St. Andrews  
St. Andrews KY16 9SS, UK

 The ORCID identification number(s) for the author(s) of this article can be found under <https://doi.org/10.1002/adom.202102065>.

© 2021 The Authors. Advanced Optical Materials published by Wiley-VCH GmbH. This is an open access article under the terms of the Creative Commons Attribution License, which permits use, distribution and reproduction in any medium, provided the original work is properly cited.

DOI: 10.1002/adom.202102065

SERDS and has already been successfully applied to a number of Raman applications largely in biomedical studies.<sup>[16–18]</sup>

Here, we show that WMRS is in fact an effective approach on samples that include metals. As an example, we employ this technique to probe a fascinating aspect of molecular strong coupling, a new field that spans physics, chemistry, and materials science and that promises to add cavity quantum electrodynamics to the chemistry/materials toolkit.<sup>[19–23]</sup> The key concept in this new area, one that has come to be known as polaritonic chemistry,<sup>[19–21,23–27]</sup> is that large ensembles of molecules placed inside an optical microcavity (or other confined light field) may exchange energy with an electromagnetic mode of the microcavity, leading to the formation of new hybrid states known as polaritons.

Strong coupling between molecular vibrations and a microcavity mode was reported in 2015 by Shalabney et al.,<sup>[23]</sup> and since then a number of investigations of vibrational strong coupling have appeared.<sup>[22,23,28–30]</sup> Of particular relevance here is another work, also from Shalabney et al. who reported that a large Rabi splitting could be seen in the Raman scattering signal from molecules strongly coupled to the infrared mode of a planar microcavity.<sup>[31]</sup>

In what follows, we first compare the Raman signals obtained using both conventional and wavelength-modulated Raman spectroscopy, using samples that comprise thin films of the materials we will use later; gold as the metal with which to make the mirrors of our planar Fabry-Perot microcavities, that is, to make the confined light fields, and the polymer PMMA for the molecular vibrations—PMMA has a high density of the C=O bond, and a molecular vibrational resonance at  $1732\text{ cm}^{-1}$  that has been employed to good effect in strong coupling experiments.<sup>[22,23,28–30]</sup> We then explore two strong coupling systems: First, we probe strong coupling in planar microcavities using WMRS; second, we then focus on another proven system, that of strong coupling molecular vibrations to confined light fields arising from surface plasmon modes.<sup>[29]</sup>

## 2. Results and Discussion

In **Figure 1**, we show the two types of structure we consider here to create confined light fields. On the left (a) is a standard planar microcavity that is formed of two semi-transparent 30 nm gold mirrors on a silicon substrate. The cavity material is a thin film, made by spin coating the polymer PMMA. To ensure that the lowest order waveguide mode is resonant with the  $1732\text{ cm}^{-1}$  vibrational mode of the C=O bond, we chose a thickness for the cavity of  $\approx 2\text{ }\mu\text{m}$ . The middle panel (b) shows a planar gold layer on a silicon substrate overlain by a thin film of PMMA. The gold film here is in the form of a grating, a 1D stripe array. We employed a grating structure so as to allow grating coupling to be used to map the dispersion of the surface plasmon mode using angle-resolved infrared transmittance.<sup>[29,32,33]</sup> Further details of sample fabrication are given in Experimental Section and Figures S2 and S3, Supporting Information.

The right hand panel (c) of **Figure 1** shows two spectra associated with the PMMA. The red curve shows the infrared transmission spectrum of a  $2\text{ }\mu\text{m}$  thick PMMA layer on a silicon substrate. The spectrum was acquired using Fourier transform infrared spectroscopy (FTIR); details are given in Experimental Section. Of particular interest here is the strong absorption at  $1732\text{ cm}^{-1}$  corresponding to the C=O stretching mode.<sup>[34,35]</sup> It is this vibrational resonance that was the subject of the pioneering work on the effect of strong coupling on vibrational resonances.<sup>[23]</sup> The black curve in **Figure 1c** is an example of a Raman spectrum, acquired using a laser pump wavelength of  $532\text{ nm}$ , from a  $2\text{ }\mu\text{m}$  thick layer of PMMA, again on a silicon substrate. Many of the features that appear in the FTIR spectrum also appear in the Raman spectrum, but their relative strength varies, reflecting the different selection rules appropriate for Raman and infrared absorption processes.<sup>[5]</sup>

Before looking at Raman spectra acquired from samples based on both the microcavity and surface plasmon structures shown in **Figures 1a** and **1b**, respectively, it is useful to compare the standard and wavelength-modulated Raman approaches

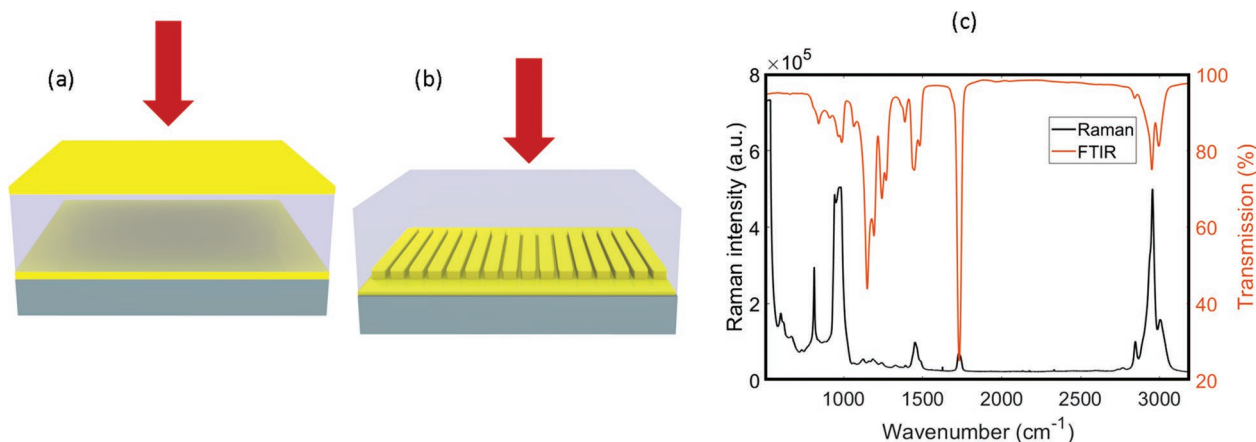
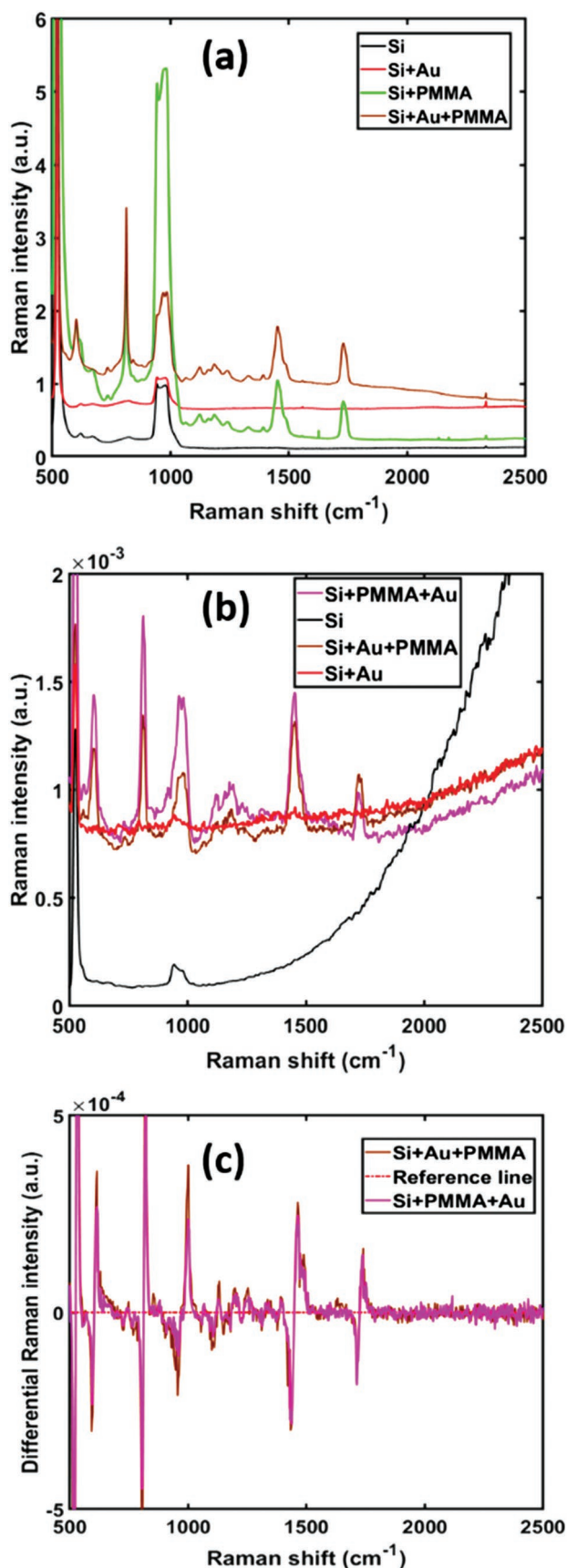


**Figure 1.** Schematics. Left: a) A planar optical microcavity comprising two semi-transparent gold mirrors on a silicon substrate. The mirrors are separated by a  $2\text{ }\mu\text{m}$  thick layer of the polymer PMMA; a cartoon of the PMMA chemical repeat unit is shown inside the cavity. The pump laser for Raman measurements is incident from above (red arrow). Middle: b) A 1D metal grating supports a surface plasmon mode. The stripe array nature of the gold film allows grating coupling to the surface plasmon mode for FTIR measurements. The thin layer of gold was added to the bottom of 1D metal grating for Raman measurements in reflection mode. Right: c) A Raman spectrum (black) of a bare PMMA film on a silicon substrate, and a transmission spectrum (orange) of a similar film.



by looking at the different materials involved. In **Figure 2**, we show three panels. In the top panel (a), we show standard Raman spectra acquired with a commercial set-up (Horiba Xplora), employing a laser pump wavelength of 532 nm, exposure time 30 s, and laser power 75 mW; four spectra are shown. The Raman spectrum of the bare silicon substrate is shown as a black line. The two clear Raman peaks at  $\approx 500$  and  $\approx 1000 \text{ cm}^{-1}$  are due to silicon.<sup>[36]</sup> The red curve is the Raman spectrum from a sample that comprised a 30 nm thick layer of gold deposited on the silicon substrate; notice here that the strength of the Si peaks has been suppressed and that there is now a significant background signal. The green curve corresponds to a sample made from a 2  $\mu\text{m}$  film of PMMA on Si; the silicon features are now strong again and a number of other prominent features associated with PMMA are visible; these include: the previously mentioned C=O stretch mode at  $1732 \text{ cm}^{-1}$  and the  $\text{CH}_3$  vibrational resonances at  $\approx 1445 \text{ cm}^{-1}$ .<sup>[34,35]</sup> The brown curve is for a sample where a layer of gold was inserted between the silicon and the PMMA. The effect of adding the top gold layer has been to reduce the strength of the silicon features and to increase the background level; this is the background signal we wished to avoid.

In the middle panel (b) of **Figure 2**, we show spectra acquired with our home-built wavelength-modulated Raman setup, but here operating in standard mode, employing a laser pump wavelength of 785 nm, at 100 mW power and with a  $1.0 \mu\text{m}$  spot size at the sample plane, with 1 s integration time per spectrum. Data from a bare silicon substrate are again shown as a black curve. We see that there is a very marked difference with the spectrum acquired for the 785 nm laser pump, panel (b), and that acquired for a 532 nm laser pump wavelength, panel (a). In particular, there is a striking background signal for the 785 nm pump, a background whose strength increases with increasing Raman shift. This signal is well known and arises from fluorescence from the silicon when illuminated at 785 nm.<sup>[37]</sup> The data from the silicon + gold (red) sample shows few if any discernible features owing to a strong background level. (Notice how the presence of the gold has strongly attenuated the silicon Raman features, but not completely eliminated the silicon fluorescence.) The spectra for silicon + PMMA + gold (magenta) and silicon + gold + PMMA (brown) both show features that can be associated with PMMA, but again, there is a very significant background level to contend with. The lower panel (c) shows the differential Raman signal acquired for the same samples as in panel (b) and using the same set-up, but this time using the wavelength-modulated technique (see Experimental

**Figure 2.** Raman spectra for different material combinations. Top: a) Standard Raman spectra acquired using a laser pump wavelength of 532 nm; the spectra are: bare silicon substrate (black), Si substrate + gold layer 30 nm thick (red), Si substrate + PMMA layer 2  $\mu\text{m}$  thick (green), and Si substrate with 30 nm gold layer followed by 2  $\mu\text{m}$  PMMA layer (brown). Middle: b) Standard Raman spectra acquired using a laser pump wavelength of 785 nm; the spectra are: silicon substrate (black), Si substrate + gold layer 30 nm thick (red), Si substrate with 30 nm gold layer followed by 2  $\mu\text{m}$  PMMA layer (brown), and Si substrate + 2  $\mu\text{m}$  PMMA layer with 30 nm of gold on top (magenta). Lower: c) The WMRS differential spectra for two samples: Si substrate with 30 nm gold layer followed by 2  $\mu\text{m}$  PMMA layer (brown); Si substrate + 2  $\mu\text{m}$  PMMA layer with 30 nm of gold on top (magenta).

Section for details). Here, we have plotted data for just two of the samples, those most relevant to the work that follows below. In magenta, we show the differential Raman spectrum for the silicon + PMMA + gold sample; in brown, we show the differential Raman spectrum for the silicon + gold + PMMA sample. The use of the differential technique has removed the background signal, as desired. In addition, the spectral features associated with the Raman modes are no longer peaks; the signal is instead differential in nature so that the position of the modes may be found from the zero-crossing points. We note that although Figure 2 shows that by using WMRS the background has been significantly reduced, all of the key features visible via WMRS were also visible via the standard Raman approach; this can be seen below by comparing panels (e) and (f) of Figure 3.

Having established the use of wavelength-modulated Raman spectroscopy to look at the vibrational modes of thin polymer films, we next set out to see if this technique could be used to help us explore strong coupling. The strong coupling of a molecular resonance and a confined light field has been the subject of intensive recent investigation.<sup>[19–21,23–27,38,39]</sup> Here, specifically, we wanted to see if WMRS could help us understand how the Raman fingerprint of a molecular vibrational resonance might be altered when the vibrational resonance is strongly coupled with a confined light field. Only two previous experimental reports concerning this are available, and they present very different results. Shalabney et al. presented Raman spectra from which they inferred a very significant signature of a lower polariton, at an energy difference from the bare

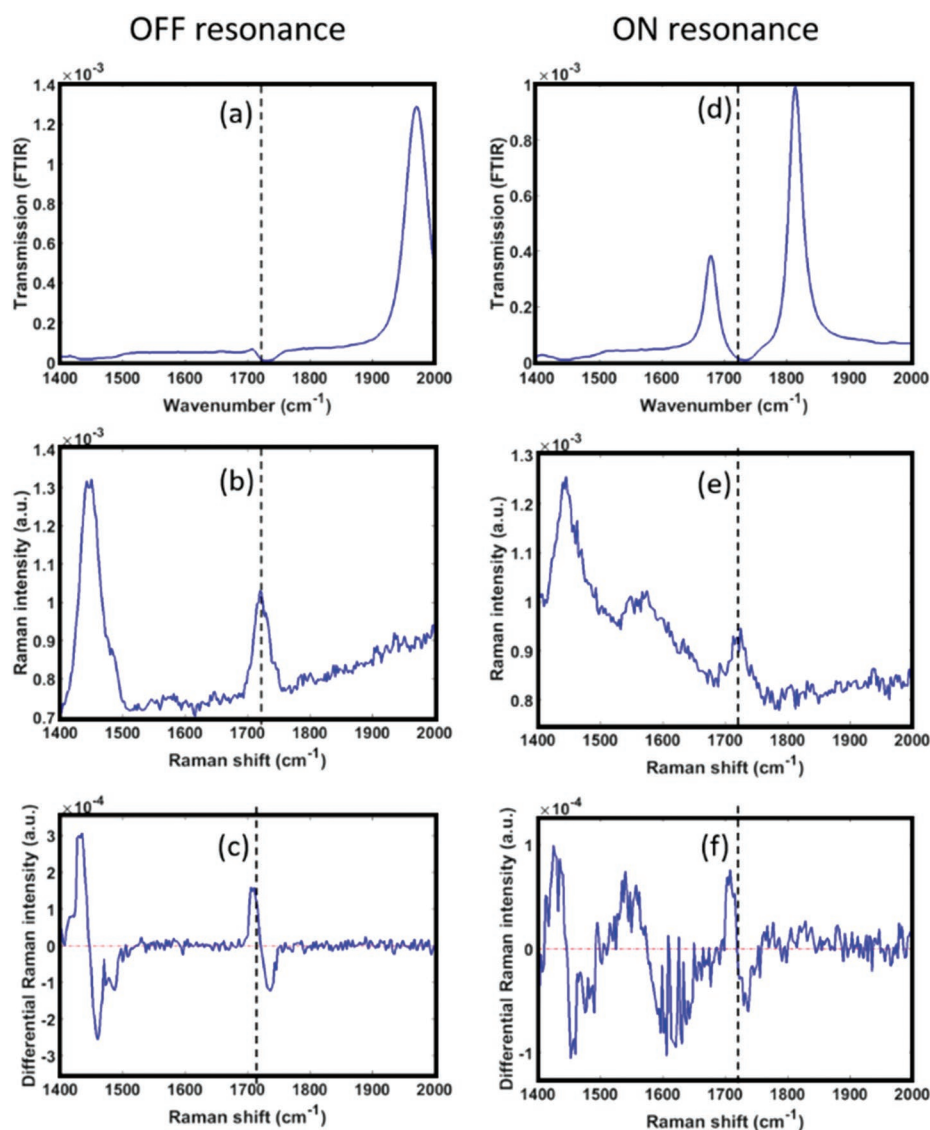


**Figure 3.** FTIR and Raman spectra from microcavity. Left section of the figure focuses on OFF-resonance microcavity. a) FTIR transmission plot at angle  $0^\circ$ . The thickness of PMMA is  $1.5 \mu\text{m}$ . Thinner cavity was prepared to get the first order cavity mode far from C=O vibrational mode which appears at around  $1732 \text{ cm}^{-1}$ . b) (Unmodulated) Standard Raman signal of the structure. c) Wavelength-modulated Raman signal. ON-resonance: d) FTIR dispersion plot at angle  $0^\circ$ . The splitting of the mode shows that the system is in strong coupling. e) (Unmodulated) Standard Raman spectra. f) Wavelength-modulated Raman spectra. The addition feature around  $1590 \text{ cm}^{-1}$  can be seen in ON resonance case. The vertical dashed black line indicates the C=O vibrational mode.

molecular resonance that was twice that associated with the lower polariton seen in FTIR from the same sample.<sup>[31]</sup> A flurry of subsequent theoretical activity did not manage to resolve this discrepancy between the position of the lower polariton as inferred from Raman and FTIR.<sup>[38,39]</sup> Since then, another report on Raman scattering and strong coupling found that the effect of strong coupling on the same vibrational bond investigated by Shalabney et al. was much more modest, leading primarily to change in line-shape.<sup>[40]</sup>

In the work reported here, we make use of two kinds of confined light fields, those associated with the modes of planar microcavities (see Figure 1a), and the surface plasmon modes associated with metal surfaces (see Figure 1b). We first look at the planar microcavity.

To investigate whether strong coupling influences the Raman fingerprint of molecules strongly coupled to the fundamental (first-order) mode of a Fabry–Perot microcavity, we made use of two samples with thicknesses of 1.5 and 2.0 microns. At a thickness of 1.5 microns, the cavity resonance is  $<2500\text{ cm}^{-1}$ , well away from the vibrational C=O stretch mode at  $1732\text{ cm}^{-1}$ ; we refer to this as the OFF-resonance sample. For the 2.0 micron thick sample, the cavity mode matches that of the vibrational resonance; we refer to this as the ON-resonance sample. The results of measurements on the OFF- and ON-resonance samples are shown in Figure 3, where the left-hand column is for the OFF-resonance sample, the right-hand column for the ON-resonance sample.

The top row of Figure 3, panels (a) and (d) show FTIR transmission plots at normal incidence for the OFF- and ON-resonance PMMA-filled planar microcavities. As expected, the OFF-resonance sample shows a transmission maximum associated with a cavity resonance at  $\approx 2000\text{ cm}^{-1}$ . At the frequency of the C=O stretch resonance  $1732\text{ cm}^{-1}$ , indicated by the vertical dashed line, there is a small dip in transmission due to absorption by this vibrational resonance in the PMMA. In contrast, the ON-resonance spectrum shows a clear splitting of the cavity mode; there are now two new hybrid modes, the lower and upper polariton. The creation of these hybrid polariton modes is a result of strong coupling between the cavity mode and the C=O vibrational resonance. Further details about meeting the strong coupling criterion are given in Sections S4 and S5, Supporting Information.

Standard Raman spectra are shown in the middle row, panels (b) and (e). Comparing the standard Raman spectra for OFF- and ON-resonance samples, panels (b) and (e), we see that the Raman peaks evident in the OFF-resonance sample are also present in the ON-resonance sample. In addition, there appears to be an extra feature, albeit rather weak, at  $\approx 1590\text{ cm}^{-1}$ .

Wavelength-modulated Raman spectra are shown in the lower row, panels (c) and (f), and now, in the WMR spectrum, the difference between the OFF-resonance case (panel c) and the ON-resonance case (panel f) is clearer; an extra zero-crossing is evident at  $\approx 1590\text{ cm}^{-1}$  in the ON-resonance case. This extra Raman feature is similar to that seen by Shalabney et al.<sup>[31]</sup> in a very similar microcavity; it is a feature that does not appear in the OFF-resonance sample. However, this  $\approx 1590\text{ cm}^{-1}$  feature is not coincident with the spectral position of the lower polariton seen in FTIR data at  $\approx 1675\text{ cm}^{-1}$ , panel (d). This difference in frequency was also noted by Shalabney et al.,<sup>[31]</sup> as was

the lack of a Raman feature associated with the upper polariton. To investigate this feature further, we made use of a different Raman setup (Horiba Xpolra) that employed a different pump wavelength (532 nm, rather than 785 nm), a different numerical aperture objective (0.55 rather than 0.9), and a different pump intensity (75 mW with  $0.5\text{ }\mu\text{m}$  spot size, rather than 100 mW with  $1.0\text{ }\mu\text{m}$  spot size). The results for the  $4.7\text{ }\mu\text{m}$  pitch grating structure are shown in Figure S11, Supporting Information. The data show that where we see the  $1590\text{ cm}^{-1}$  feature using the 785 nm Raman setup (Figure 3), we also see it with the 532 nm set-up (Figure S11, Supporting Information). The  $1590\text{ cm}^{-1}$  feature thus appears not to be specific to the measurement system used. Before discussing these results further, it is interesting to first exploit another capability of our Raman spectroscopy set-up, that of recording a spatial map.

Returning now to the discussion of the cavity results, we recorded standard Raman and wavelength-modulated Raman signals at different positions on our samples, data being recorded every  $0.5\text{ }\mu\text{m}$  along a line scan; data of this type are shown in Figure 4. In Figure 4a, the Raman features of PMMA for the OFF-resonance cavity are reasonably clear; the WMR spectra in Figure 4c for the same sample are also very well defined. Recall that in WMR spectra, Raman peaks are indicated by zero crossings of this differential signal; this is clearly seen in these data for the vibrational resonances of PMMA and for silicon. For each resonance, as one goes up in energy, that is, moves to higher wave-numbers, the signal is first positive (yellow) and then negative (blue). Similar data for the ON-resonance sample are shown in Figure 4b,d. The standard Raman features, Figure 4b, are rather overwhelmed by what appears to be a strong background signal in the middle of the figure, perhaps due to some sample imperfection or dust; it is not clear whether the feature at  $\approx 1590\text{ cm}^{-1}$  is a Raman peak or not. The power of the WMR approach becomes clear when looking at the data in Figure 4d; no trace of this background remains, and it is now clear that the feature at  $\approx 1590\text{ cm}^{-1}$  is a Raman signal, the transition from yellow to blue signal being evident as one goes from the low energy side of the feature to the high energy side. At a spatial position of approx 4.5 microns in Figure 4d, the sign of the differential signal changes. Up to 4.0 microns, the signal is first positive, then negative as the energy increases; at 5.0 microns, the negative comes before the positive. Which sign the differential signal takes is determined during the data processing for the WMR data (see Experimental Section). Noise in the spectra can lead to the sign of the modulated signal being flipped. There is thus no physical significance associated with the sign changes seen in panel (d).

Let us focus on the  $\approx 1590\text{ cm}^{-1}$  feature, the one that Shalabney et al.<sup>[31]</sup> associated with a lower polariton. Since the original observation by Shalabney et al.,<sup>[31]</sup> two theoretical investigations have been carried out, but could not explain this observation.<sup>[38,39]</sup> Returning now to our data, the fact that we see a Raman feature at  $\approx 1590\text{ cm}^{-1}$  only for the ON-resonance sample and not the OFF-resonance sample leads to a temptation to think that this feature is associated with a lower polariton. However, we still have to explain why the Raman feature at  $\approx 1590\text{ cm}^{-1}$  is so far removed from the position of the lower polariton as seen in FTIR, for which the lower polariton energy is  $\approx 1675\text{ cm}^{-1}$ . Then there is the recent work of Wonmi and

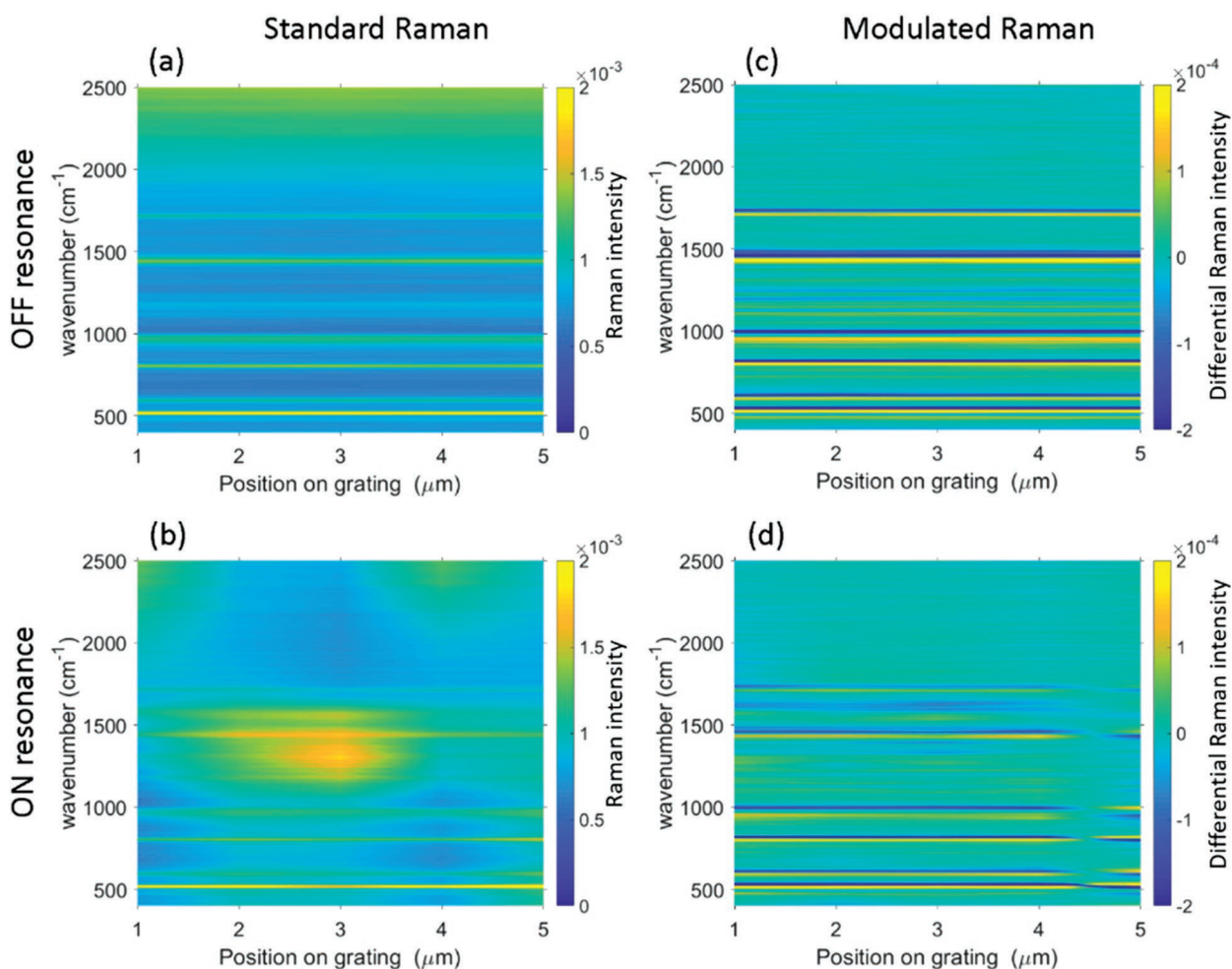


**Figure 4.** Spatial maps of Raman data from planar microcavities. a) Standard Raman spectra from the OFF-resonance cavity are shown as a function of position along a 5 micron line-scan. b) Wavelength-modulated Raman spectra from the OFF-resonance cavity. c) Standard Raman spectra from the ON-resonance cavity. d) Wavelength-modulated Raman spectra from the ON resonance cavity. The additional feature is seen around 1590 cm<sup>-1</sup>. The color scale indicates the strength of the Raman signal.

Simpkins<sup>[40]</sup> who also explored Raman scattering in the context of vibrational strong coupling of PMMA in a planar optical cavity. They found that only small changes in the Raman peak associated with the C=O bond could be associated with strong coupling. Then, we should also consider the possible influence of the dispersion of the polariton modes in our systems. Vurgaftman et al.<sup>[41]</sup> recently investigated the effect of the dispersion of polaritons in the context of trying to modify chemical reactions through strong coupling of vibrational modes, basing their discussion on a density of states argument. The dispersion of the polaritons as a function of in-plane wavevector is well known, and an example for the ON-resonance sample shown here can be seen in Figure S6, Supporting Information, where as expected we see that the frequency of the lower polariton is not constant with wavevector. In common with most Raman measurements, we used a relatively high NA objective to collect the Raman scattered signal, the effect of which will be to collect light from different parts of the polariton branch at different energies. We might expect that the net result will thus be to smear out, that is, to make less obvious any Raman signal that

might originate from a polariton.<sup>[41]</sup> The fact that  $\approx 1590$  cm<sup>-1</sup> matches that of “damaged” PMMA is also of concern; the issue of whether damage to the PMMA is the cause of these additional features will be discussed further below.

To explore the question of Raman scattering and strong coupling further, we used the wavelength-modulated Raman approach to look at strong coupling between the same vibrational resonance in PMMA (C=O at  $\approx 1732$  cm<sup>-1</sup>) and a surface plasmon mode. Surface plasmon modes are trapped surface modes that cannot usually be coupled to incident radiation<sup>[42,43]</sup>; they have too much momentum in the plane of the surface that supports them. Some form of momentum matching is required, and two common techniques are very effective; Memi et al.<sup>[32]</sup> made use of prism coupling; here we adopted a second well known approach, that of grating coupling.<sup>[44]</sup> We chose to use metal stripe gratings<sup>[45]</sup> made of gold, as shown in Figure 1b. These 1D arrays have been used to great effect before to study strong coupling between surface plasmons and molecules, both excitonic<sup>[46]</sup> and vibrational.<sup>[29]</sup> Further details of sample fabrication are given in Experimental Section and Supporting Information.

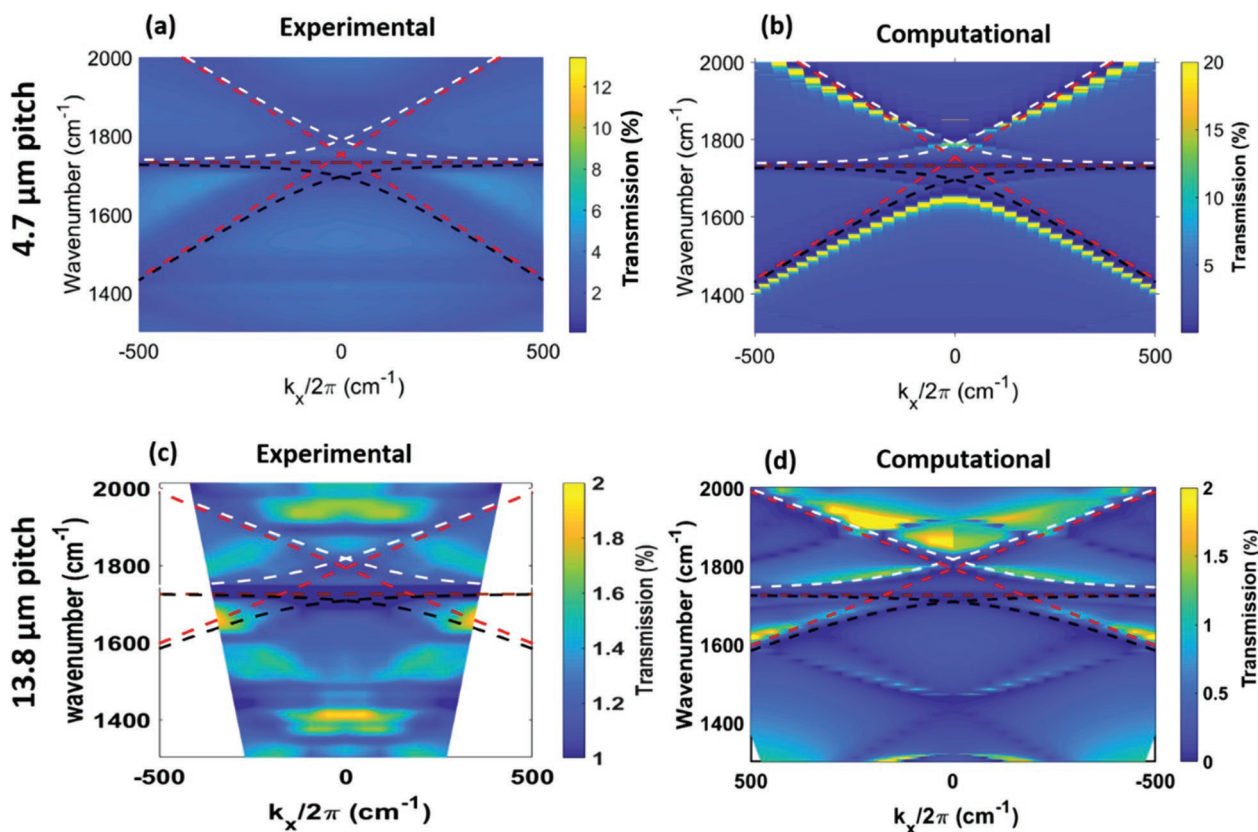


**Figure 5.** Surface plasmon dispersion with the plane of incidence orthogonal to the grating grooves, and the incident electric field in the plane of incidence. Left side of the figures shows experimentally calculated transmittance data and right side shows computationally calculated transmittance data. The period of the grating for top row is 4.7  $\mu\text{m}$  and for bottom row is 13.8  $\mu\text{m}$ , with a 1.0  $\mu\text{m}$  gap between metal stripes. The PMMA thickness is 1.0  $\mu\text{m}$ . Also shown are the calculated positions (colored dashed lines) of the polariton branches from the coupled oscillator model: lower polariton (white), grating mode (red), and upper polariton (black). The horizontal dashed red lines indicate the energy of the C=O (1732  $\text{cm}^{-1}$ ) vibrational resonance. a) The measured infrared transmittance of the 4.7  $\mu\text{m}$  sample shown is plotted as a function of frequency ( $\text{cm}^{-1}$ ) and in-plane wavevector ( $k_x$ ). b) Numerically modeled data using COMSOL Multiphysics. The calculated transmittance is shown as a function of frequency ( $\text{cm}^{-1}$ ) and in-plane wavevector  $k_x$ . c) The measured infrared transmittance of the 13.8  $\mu\text{m}$  sample is plotted as a function of frequency ( $\text{cm}^{-1}$ ) and in-plane wavevector ( $k_x$ ). d) The calculated transmittance is shown as a function of frequency ( $\text{cm}^{-1}$ ) and in-plane wavevector  $k_x$ . The Rabi splitting for both the cases is 90  $\text{cm}^{-1}$ .

We chose two samples, one with a period of 4.7  $\mu\text{m}$  and another with a period of 13.8  $\mu\text{m}$  for our gold stripe array; this choice ensured that grating coupling to the surface plasmon mode could be achieved in the spectral range we required (see Figure 5). The samples were chosen to couple C=O vibrational mode with first-order and third-order of scattered plasmonic mode with 4.7  $\mu\text{m}$  pitch and with 13.8  $\mu\text{m}$ , respectively.

We used FTIR measurements made as a function of angle to compile a dispersion plot, that is, a plot of transmittance as a function of energy (wavenumber) and in-plane wavevector ( $k_x$ ). The left-hand panel in Figure 5 shows experimental data acquired in this way. The maximum polar angle for these data is 12°. The frequency of the vibrational resonance of interest here is shown as a brown dashed line. To help identify the features seen in this plot, it is useful to compare them with data calculated using COMSOL (See Experimental Section); such data are shown in the right-hand column. We also used a coupled oscillator model (see Section S5, Supporting Information) to calculate the position of the polariton bands, as indicated on the figure; the black dashed line is for the upper polariton band, the white dashed line is for the lower polariton band.

The dashed lines are repeated on the experimental data shown in panel (a) and (c) as well as on computational data shown in panel (b) and (d) of Figure 5. Doing this allows us to see the position of the grating scattered surface plasmon mode, indicated by the dashed red line. The anti-crossing of the surface plasmon mode with the vibrational resonance to produce two hybrid polariton bands is now apparent.

To check whether we are in the strong coupling regime, we need to determine whether  $\Omega_a > (\gamma + \kappa)/2$ , where  $\Omega_a$  is the coupling strength (Rabi splitting) and  $\kappa$  and  $\gamma$  are the widths of the plasmon mode and the molecular resonance.

We used the same coupled oscillator model as for the cavity, and found the coupling strength  $\Omega_a$  to be  $90 \pm 30 \text{ cm}^{-1}$  for both, 4.7  $\mu\text{m}$  pitch and 13.8  $\mu\text{m}$  pitch samples. The C=O molecular resonance width,  $\gamma$ , is 60  $\text{cm}^{-1}$  ( $\pm 5 \text{ cm}^{-1}$ ), and the plasmon mode linewidth,  $\kappa$ , 60  $\text{cm}^{-1}$  ( $\pm 5 \text{ cm}^{-1}$ ). Based on the criterion that for strong coupling we require  $\Omega_a > (\gamma + \kappa)/2$ , this is satisfied for both the 4.7 and 13.8  $\mu\text{m}$  pitch samples<sup>[47,48]</sup>

We now turn to the Raman results. For the 1D array, we recorded standard Raman and wavelength-modulated Raman signals at different positions along the sample, data again

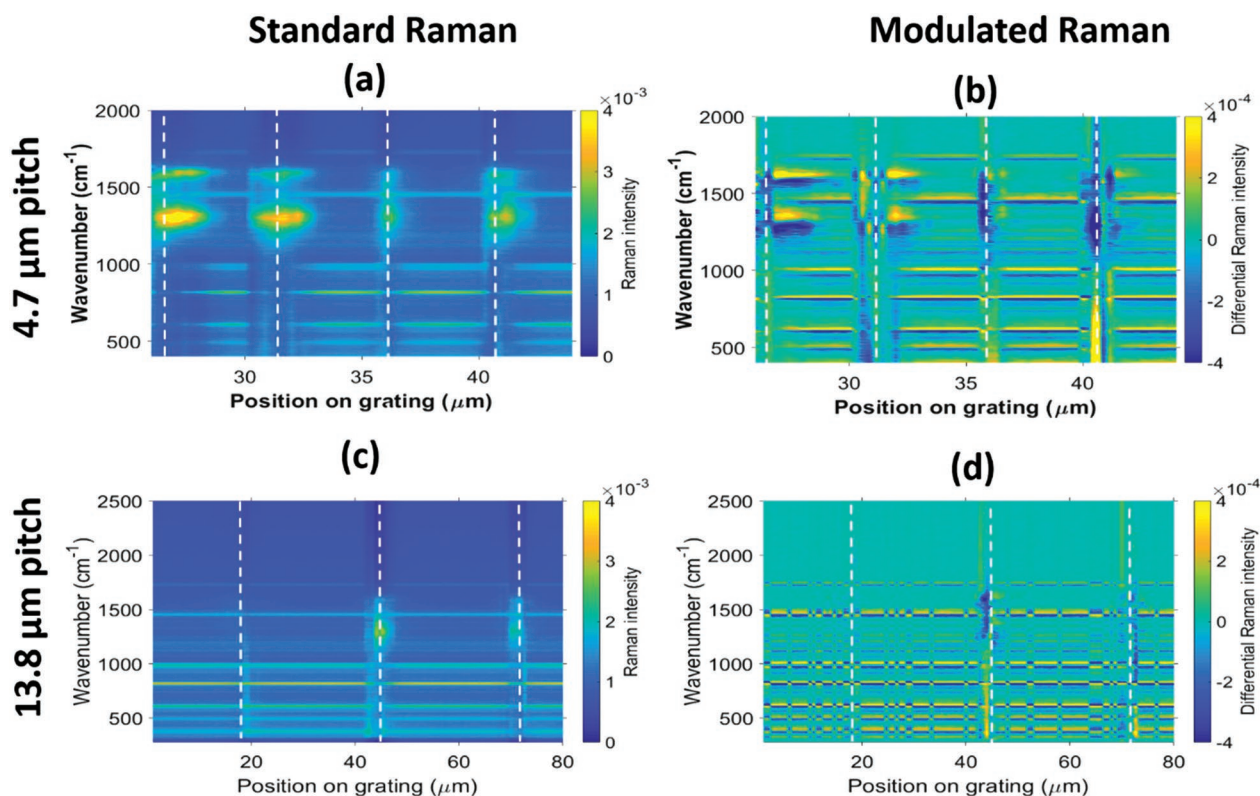


**Figure 6.** Spatial maps of Raman data from grating 4.7  $\mu\text{m}$  pitch. a) Standard Raman spectra of grating sample 1b. b) Wavelength-modulated data with respect to position on grating. The separation between two successive data sampling points is 0.5  $\mu\text{m}$ . The grating pitch is 4.7  $\mu\text{m}$  and 1  $\mu\text{m}$  gap. 13.8  $\mu\text{m}$  pitch. c) Standard Raman spectra of grating sample 1b. d) Wavelength-modulated data with respect to position on grating. The separation between two successive data sampling points is 0.5  $\mu\text{m}$ . The initial 18 positions were covered outside the grating region. The vertical white dashed lines show the periodic grating of the structure.

being recorded every 0.5  $\mu\text{m}$  nm along a line scan normal to the stripes. The top row of Figure 6 shows Raman spectra for the 4.7  $\mu\text{m}$  pitch sample and bottom row shows spectra for the 13.8  $\mu\text{m}$  pitch sample. Figure 6a,c shows standard Raman spectra as a function of position along the grating. As for the microcavity (Figure 4), data are plotted as a colour scale, that is, the colour indicates the strength of the signal, the abscissa ( $x$ -axis) indicates the position, and the ordinate ( $y$ -axis) indicates the wavenumber. The dashed white lines indicate the approximate positions of the grating grooves, that is, those regions of the stripe array without metal.

These standard Raman spectra show a number of features. In the regions between the grooves we see the usual Raman features associated with PMMA. In regions in the vicinity of the grating grooves, the data are very different; we see what look like extra features between  $\approx 1200$  and  $\approx 1600$   $\text{cm}^{-1}$ . The value of the WMR technique now becomes clear from the wavelength-modulated Raman data shown in Figure 6b,d. In Figure 6b, for the 4.7  $\mu\text{m}$  pitch sample, it is now clear that there are two additional Raman features, one at  $\approx 1590$   $\text{cm}^{-1}$ , and one at  $\approx 1320$   $\text{cm}^{-1}$ . These features are not well confined to the gap regions, although they do appear to be associated with the gaps. This lack of resolution may be the result of a combination of the pump laser spot size (1  $\mu\text{m}$ ) being comparable to the gap size of the grating (1  $\mu\text{m}$ ), and greater than the step size of the spatial scan (0.5  $\mu\text{m}$ ); there might also be problems associated

with scattering from imperfections in the grating grooves, perhaps due to uneven lift-off in the fabrication process.

In Figure 6d, for the 13.8  $\mu\text{m}$  pitch sample, no additional features are immediately evident in the Raman spectra, either in the region of the gaps, or elsewhere. This was true for many, but not all of the samples/measurements we made. One possible explanation is that while the grating coupled plasmon mode we see for the 4.7  $\mu\text{m}$ , this pitch is first-order; for the 13.8  $\mu\text{m}$  pitch, it is a third order scattering that renders the mode visible. We also note that for the 4.7  $\mu\text{m}$  pitch sample, the de-tuning at  $k = 0$  is very small, whereas for 13.8  $\mu\text{m}$ , it is more significant. If we analyze the line spectra in the region of the grooves, then we find that they do show additional Raman features at  $\approx 1590$  and  $\approx 1320$   $\text{cm}^{-1}$  (see Figures S9 and S10, Supporting Information). Notice also that in these data (Figure 6b,d) as for the cavity (Figure 4b), the sign of the differential signal often swaps. As before, we attribute this to the WMR data processing, and there is thus no physical significance associated with the sign changes seen in panels (b) and (d).

### 3. Summary and Discussion

We have shown that wavelength-modulated Raman spectroscopy is a powerful technique with which to probe Raman scattering in molecular samples where the desired signals are

degraded by fluorescence from metals. We applied this technique to probe the strong coupling of vibrational modes and confined light fields, using the photonic modes of planar microcavities and the surface plasmon modes of metallic diffraction gratings as the confining light fields, and the C=O double bond in the polymer PMMA as the molecular resonance.

For the planar microcavities, we found an additional feature in the Raman spectrum, beyond that usually observed for PMMA, occurring at  $1590\text{ cm}^{-1}$ . This feature appeared when the cavity was tuned to be on-resonance with the the C=O ( $1730\text{ cm}^{-1}$ ) vibrational mode; it was not observed for an off-resonance cavity sample. The additional feature at  $1590\text{ cm}^{-1}$  is consistent with the previous work of Shalabney et al, and those authors attributed this extra feature to the lower polariton arising from hybridization of the C=O molecular resonance with the cavity mode. Such an explanation might apply here, but there are a number of reasons for doubt.

First, as noted by Shalabney et al., the Raman feature at  $1590\text{ cm}^{-1}$  is not matched in energy with the position of the lower polariton seen in FTIR, which in our case occurs at  $\approx 1675\text{ cm}^{-1}$ . There has been no theoretical prediction/understanding yet of this discrepancy. Another recent report suggests that any changes in Raman spectra arising from strong coupling in this type of sample is likely to be very small, producing primarily a change in the shape of the Raman peak, rather than a significant shift in frequency.<sup>[40]</sup> It is thus important to consider alternative explanations for this  $1590\text{ cm}^{-1}$  feature, and damage to the PMMA layer is perhaps the prime candidate. Shalabney et al. did consider this possibility, and conducted tests on bare polymer films to try and ensure they were working below any photo-damage threshold. Nonetheless, we find it striking that our on-resonance sample shows a Raman feature at  $1590\text{ cm}^{-1}$ , similar to that which has been shown to arise from thermal degradation,<sup>[49]</sup> as determined from thermal analysis FTIR, and from ion-implantation,<sup>[50]</sup> as determined by Raman scattering. In the case of the ion-implantation study, the presence of extra features was found to depend on the Raman pump wavelength, but the  $1590\text{ cm}^{-1}$  feature was seen for a pump wavelength of  $785\text{ nm}$ , the wavelength used in our WMR setup. Why the extra Raman feature shows up only for the on-resonance cavity remains a mystery. We note that the pump laser we used had a high numerical aperture (NA) and is thus incident over a wide angle range, spanning several modes at laser (pump) wavelength, so the observation of this Raman feature for the on-resonance cavity is unlikely to be a consequence of being on resonance with a visible mode of the cavity. Measurements conducted using a different (standard) Raman setup and employing a different numerical aperture, see Figure S11, Supporting Information, showed a similar feature at  $1590\text{ cm}^{-1}$ . Another mystery is the absence of any Raman feature associated with an upper polariton band, although theoretical work indicates this might be expected.<sup>[39]</sup>

For the grating-coupled surface plasmon samples, we also found additional Raman features, again at  $\approx 1590\text{ cm}^{-1}$ , but also at  $1320\text{ cm}^{-1}$ , and they seem to be associated with the periodic grooves in the metal stripe arrays we used.<sup>[51]</sup> The additional features did not appear in the planar regions of these samples. We note that these features were not very reproducible, that is, they did not arise in every gap investigated and were largely

absent from the longer pitch samples we examined, despite both samples ( $4.7\text{ }\mu\text{m}$  and  $13.8\text{ }\mu\text{m}$  pitch) ostensibly being in the strong coupling regime. One possible explanation might be that the first-order coupling is likely to lead to the creation of a surface plasmon band edge that may provide an additional degree of field enhancement.<sup>[29]</sup>

Is the fact that for the grating structures the extra Raman features appear at the same frequencies as those for the planar microcavity a coincidence? (It is not clear whether a  $1320\text{ cm}^{-1}$  feature is present for the planar ON-resonance microcavity; the data are too noisy to make any claim in this regard (see Figure S7, Supporting Information). Is the  $1590\text{ cm}^{-1}$  feature a lower polariton associated with the PMMA resonance at  $1730\text{ cm}^{-1}$ , and could the  $1320\text{ cm}^{-1}$  be a lower polariton associated with the PMMA resonance at  $1450\text{ cm}^{-1}$ , or might it too be due to damage?<sup>[50]</sup> More work is needed to answer these questions.

Overall, the results of our investigation are inconclusive regarding any change in Raman scattering as a result of the strong coupling of molecular vibrational modes. On the one hand, our results might be interpreted as showing features associated with photo-damage to the polymer, rather than providing evidence for polaritons formed as a result of strong coupling. On the other hand, the fact that the extra features we see are only evident for samples in the strong coupling regime might be construed as indicating otherwise, and if one could gain some confidence that the  $1590\text{ cm}^{-1}$  feature is a lower polariton, we still have to account for the mismatch between the energy of the Raman feature and the FTIR feature.

Our aim in presenting these rather confusing results is to spur others to investigate these effects more deeply so as to help resolve these intriguing questions. Further investigations are underway to look in more detail at the spatial dependence of the Raman scattering signal for the grating-coupled surface plasmon structures. Looking ahead, we can identify several areas worthy of exploration. First, it would be advantageous to combine some kind of independent assessment of any damage to the polymer, perhaps by carrying out control experiments in which damage is induced thermally<sup>[49]</sup> so as to provide a direct comparison. Second, a worthwhile alternative might be to change to a different vibrational system, for example, moving away from a polymer and making use of a more robust system. For such a study, a resonance that is both IR active and Raman active is needed; such a situation applies to the  $1730\text{ cm}^{-1}$  mode of PMMA and is one of the reasons this material was attractive for such work in the first place. Third, it would be interesting to try and measure the Raman signal in an angle-resolved way, so as to better compare the Raman signal with the measured dispersion. Finally, during submission of this paper, Takele et al.<sup>[52]</sup> showed that even in the vibrational strong coupling regime, changes in Raman spectra may result from surface enhancement (SERS) effects and do not necessarily result from strong coupling.

## 4. Experimental Section

*Wavelength-Modulated Raman Spectroscopy:* The experiments were carried on the similar Raman system as described in the previous work.<sup>[53,54]</sup> Five Raman spectra were acquired over  $5\text{ s}$  with  $1\text{ s}$  integration time for each spectrum, at different excitation wavelengths with the

central wavelength at 785 nm and a tuning step of 0.2 nm. Using principal component analysis, these five Raman spectra were reconstructed into one single wavelength-modulated Raman (WMR) spectrum. In such a single WMR spectrum, zero-crossings are equivalent to peak positions while the peak-to-valley corresponds to the peak intensity in a standard Raman spectrum.

**Optical Microcavities:** The cavity mirrors were both made of gold by e-beam assisted evaporation and each had a nominal thickness of 12 nm. The PMMA (molecular weight 950K) was spin coated from a solution diluted in 11% Anisole to achieve a layer thickness of 2  $\mu\text{m}$ . The microcavity was formed on a silicon substrate that had a minimal oxide thickness layer.

**Grating Fabrication:** 100 nm of thin gold film was deposited on silicon substrate, so that the gold mirrors were 100 nm thick, with a calculated reflectivity of greater than 0.95. Later, 1D grating structures were produced using electron beam lithography. Briefly, an e-beam resist (PMMA: 950K A9) was spun (4000 rpm) onto a 20 mm square silicon wafer substrate to obtain a thickness of  $\approx 400$  nm. The substrate was then heated to 180 $^{\circ}$  C for 10 min to remove the solvent. For the electron beam lithography, a  $\approx 20$  nA beam current was used to write the desired pattern. Following exposure, the resist was developed (MEK+MIBK+IPA) for 40 s. A thin 100 nm gold film was then deposited by thermal evaporation, followed by a lift-off process to leave the desired gold stripe grating (see Figure 1b).

**FTIR Measurements:** The IR transmission of the samples was determined using an FTIR set-up (Bruker V80). To produce dispersion curves, spectra were acquired for a range of incident angles, typically in the range  $-12^{\circ}$  to  $+12^{\circ}$ . All measurements were performed with a spectral resolution of 8  $\text{cm}^{-1}$  and an angular resolution of 2 $^{\circ}$ . To improve the signal-to-noise, averaging over 128 scans was carried out. Sample transmittance spectra are shown in Figure 5a,c.

**Numerical Modeling:** To model the response from these structures, finite-element-modeling was employed through the use of COMSOL Multiphysics. An example in Figure 5a,c, for which the COMSOL calculations involved a modeling volume that comprised a 3  $\mu\text{m}$  layer of  $\text{CaF}_2$  overlain with a 30 nm gold grating, covered by 1  $\mu\text{m}$  layer of PMMA and finally followed by 3  $\mu\text{m}$  layer of air. Periodic boundary conditions were added in the grating (x) direction. For the meshing, a minimum mesh element size of 0.22 nm was used, while the maximum mesh element size was 185 nm; a curvature factor of 0.2 was used to smooth the vertices so as to better represent the fabricated samples.

**Material Parameters:** For the frequency-dependent permittivity of both gold and PMMA, Drude-Lorentz

$$\epsilon(\omega) = \epsilon_b - \frac{\omega_p^2}{\omega^2 + i\gamma\omega} \quad (1)$$

and Lorentz oscillator

$$\epsilon(\omega) = \epsilon_{\infty} + \sum_j \frac{\omega_{j0}^2 f_j}{\omega_{j0}^2 - \omega^2 - i\gamma_j \omega} \quad (2)$$

models, respectively, were made use of. For gold, parameters taken from Olmon et al.<sup>[55]</sup> were used, specifically,  $\omega_p = 1.29 \times 10^{16} \text{ rad s}^{-1}$ , and  $\gamma = 7.30 \times 10^{13} \text{ rad s}^{-1}$ , with  $\epsilon_b = 1.0$ . For PMMA, single oscillator parameters from Shalabney et al.<sup>[23]</sup> were taken, specifically,  $\omega_0 = 3.28 \times 10^{14} \text{ rad s}^{-1}$ , and  $\gamma = 2.45 \times 10^{12} \text{ rad s}^{-1}$ , with  $f_0 = 0.0165$ , and  $\epsilon_b = 1.99$ . The parameters for silicon in the infrared were based on data compiled by Edwards<sup>[56]</sup> and were taken to be,  $\epsilon = 11.76 + 0.001i$ , while for air,  $\epsilon = 1.0$  was taken.

## Supporting Information

Supporting Information is available from the Wiley Online Library or from the author.

## Acknowledgements

The authors are indebted to Blake Simpkins for valuable discussions during the course of this work.

The authors acknowledge financial support from the Engineering and Physical Sciences Research Council (EPSRC) of the United Kingdom, via the EPSRC Centre for Doctoral Training in Metamaterials (Grant No. EP/L015331/1). W.L.B. acknowledges the support of the European Research Council through project photmat (ERC-2016-AdG-742222: www.photmat.eu) and the Leverhulme Trust (Grant No. 111715R).

## Conflict of Interest

The authors declare no conflict of interest.

## Data Availability Statement

Data created during this research are openly available from the University of Exeter's institutional repository at, <https://doi.org/10.24378/exe.3643>.

## Keywords

optical microcavity, plasmonics, Raman spectroscopy, vibrational strong coupling

Received: September 25, 2021

Revised: October 28, 2021

Published online:

- [1] X. Zhang, X.-F. Qiao, W. Shi, J.-B. Wu, D.-S. Jiang, P.-H. Tan, *Chem. Soc. Rev.* **2015**, *44*, 2757.
- [2] R. Saito, Y. Tatsumi, S. Huang, X. Ling, M. S. Dresselhaus, *J. Phys.: Condens. Matter* **2016**, *28*, 353002.
- [3] P. Matousek, N. Stone, *Analyst* **2009**, *134*, 1058.
- [4] G. Marucci, A. Beeby, A. W. Parker, C. E. Nicholson, *Anal. Methods* **2018**, *10*, 1219.
- [5] P. Larkin, *Infrared and Raman Spectroscopy*, 2nd ed., Elsevier BV, Oxford **2018**.
- [6] H. Xu, X.-H. Wang, M. P. Persson, H. Q. Xu, M. Käll, P. Johansson, *Phys. Rev. Lett.* **2004**, *93*, 24.
- [7] P. Johansson, H. Xu, M. Käll, *Phys. Rev. B* **2005**, *72*, 035427.
- [8] B. Auguie, A. Reigue, E. C. Le Ru, P. G. Etchegoin, *Anal. Chem.* **2012**, *84*, 7938.
- [9] D. Wei, S. Chen, Q. Liu, *Appl. Spectrosc. Rev.* **2015**, *50*, 387.
- [10] J. Zhao, H. Lui, D. I. McLean, H. Zeng, *Appl. Spectrosc.* **2007**, *61*, 1225.
- [11] T. Hasegawa, J. Nishijo, J. Umemura, *Chem. Phys. Lett.* **2000**, *317*, 642.
- [12] E. V. Efremov, J. B. Buijs, C. Gooijer, F. Ariese, *Appl. Spectrosc.* **2007**, *61*, 571.
- [13] E. C. Le Ru, L. C. Schroeter, P. G. Etchegoin, *Anal. Chem.* **2012**, *84*, 5074.
- [14] J. B. Cooper, M. Abdelkader, K. L. Wise, *Appl. Spectrosc.* **2013**, *67*, 973.
- [15] M. Mazilu, A. C. De Luca, A. Riches, C. S. Herrington, K. Dholakia, *Opt. Express* **2010**, *18*, 11382.
- [16] M. Chen, J. Mas, L. H. Forbes, M. R. Andrews, K. Dholakia, *J. Biophotonics* **2018**, *11*, e201700129.
- [17] L. Woolford, M. Chen, K. Dholakia, C. S. Herrington, *J. Biophotonics* **2018**, *11*, e201700244.

- [18] V. O. Baron, M. Chen, B. Hammarstrom, R. J. H. Hammond, P. Glynne-Jones, S. H. Gillespie, K. Dholakia, *Commun. Biol.* **2020**, 3, 236.
- [19] T. W. Ebbesen, *Acc. Chem. Res.* **2016**, 49, 2403.
- [20] K. Bennett, M. Kowalewski, S. Mukamel, *Faraday Discuss.* **2016**, 194, 259.
- [21] M. Hertzog, M. Wang, J. Mony, K. Börjesson, *Chem. Soc. Rev.* **2019**, 48, 937.
- [22] J. P. Long, B. S. Simpkins, *ACS Photonics* **2015**, 2, 130.
- [23] A. Shalabney, J. George, J. Hutchison, G. Pupillo, C. Genet, T. W. Ebbesen, *Nat. Commun.* **2015**, 6, 1.
- [24] F. Herrera, F. C. Spano, *Phys. Rev. Lett.* **2016**, 116, 238301.
- [25] J. Feist, J. Galego, F. J. Garcia-Vidal, *ACS Photonics* **2017**, 5, 205.
- [26] R. F. Ribeiro, L. A. Martínez-Martínez, M. Du, J. Campos-Gonzalez-Angulo, J. Yuen-Zhou, *Chem. Sci.* **2018**, 9, 6325.
- [27] J. Yuen-Zhou, V. M. Menon, *Proc. Natl. Acad. Sci. USA* **2019**, 116, 5214.
- [28] K. S. Menghrajani, H. A. Fernandez, G. R. Nash, W. L. Barnes, *Adv. Opt. Mater.* **2019**, 7, 1900403.
- [29] K. S. Menghrajani, G. R. Nash, W. L. Barnes, *ACS Photonics* **2019**, 6, 2110.
- [30] B. S. Simpkins, K. P. Fears, W. J. Dressick, B. T. Spann, A. D. Dunkelberger, J. C. Owrutsky, *ACS Photonics* **2015**, 2, 1460.
- [31] A. Shalabney, J. George, H. Hiura, J. A. Hutchison, C. Genet, P. Hellwig, T. W. Ebbesen, *Angew. Chem., Int. Ed.* **2015**, 54, 7971.
- [32] H. Memmi, O. Benson, S. Sadofev, S. Kalusniak, *Phys. Rev. Lett.* **2017**, 118, 126802.
- [33] W. Wan, X. Yang, J. Gao, *Opt. Express* **2016**, 24, 12367.
- [34] H. Nagai, *J. Appl. Polym. Sci.* **1963**, 7, 1697.
- [35] I. J. Luxmoore, P. Q. Liu, P. Li, J. Faist, G. R. Nash, *ACS Photonics* **2016**, 3, 936.
- [36] A. Zwick, R. Carles, *Phys. Rev. B* **1993**, 48, 6024.
- [37] S. Zhang, Y. Hou, K. Ho, B. Qian, S. Cai, *J. Appl. Phys.* **1992**, 72, 4469.
- [38] J. del Pino, J. Feist, F. J. Garcia-Vidal, *J. Phys. Chem. C* **2015**, 119, 29132.
- [39] A. Strashko, J. Keeling, *Phys. Rev. A* **2016**, 94, 023843.
- [40] W. Ahn, B. S. Simpkins, *J. Phys. Chem. C* **2021**, 125, 830.
- [41] I. Vurgaftman, B. S. Simpkins, A. D. Dunkelberger, J. C. Owrutsky, *J. Phys. Chem. Lett.* **2020**, 11, 3557.
- [42] H. Raether, *Surface Plasmons: On Smooth and Rough Surfaces and on Gratings*, Vol. 111, Springer Tracts in Modern Physics, Springer Verlag, Berlin **1988**.
- [43] *Plasmonics: Fundamentals and Applications*, Springer, New York **2007**.
- [44] R. H. Ritchie, E. T. Arakawa, J. J. Cowan, R. N. Hamm, *Phys. Rev. Lett.* **1968**, 21, 1530.
- [45] F. J. García-Vidal, L. Martín-Moreno, *Phys. Rev. B* **2002**, 66, 155412.
- [46] P. Vasa, W. Wang, R. Pomraenke, M. Lammers, M. Maiuri, C. Manzoni, G. Cerullo, C. Lienau, *Nat. Photonics* **2013**, 7, 128.
- [47] G. Zengin, T. Gschneidner, R. Verre, L. Shao, T. J. Antosiewicz, K. Moth-Poulsen, M. Käll, T. Shegai, *J. Phys. Chem. C* **2016**, 120, 20588.
- [48] P. Törmä, W. L. Barnes, *Rep. Prog. Phys.* **2015**, 78, 013901.
- [49] B. Holland, J. Hay, *Polymer* **2001**, 42, 4825.
- [50] T. Kavetsky, J. Nowak, J. Borc, J. Rusnák, O. Šauša, A. L. Stepanov, *Spectrosc. Lett.* **2016**, 49, 5.
- [51] We also investigated samples for which there was no metal in the groove regions. The WMRS data from these samples showed evidence of extra features at both  $\approx 1590$  and  $1320\text{ cm}^{-1}$ , and the calculated electric field distributions showed a local electric field enhancement at the edges of the grooves, an enhancement not apparent in similar calculations for structures similar to those reported above.
- [52] W. M. Takele, F. Wackenhut, L. Piatowski, A. J. Meixner, J. Waluk, *J. Phys. Chem. B* **2020**, 124, 5709.
- [53] M. Chen, N. McReynolds, E. C. Campbell, M. Mazilu, J. Barbosa, K. Dholakia, S. J. Powis, *PLoS ONE* **2015**, 10, e0125158.
- [54] V. O. Baron, M. Chen, S. O. Clark, A. Williams, R. J. H. Hammond, K. Dholakia, S. H. Gillespie, *Sci. Rep.* **2017**, 7, 9844.
- [55] R. L. Olmon, B. Slovick, T. W. Johnson, D. Shelton, S.-H. Oh, G. D. Boreman, M. B. Raschke, *Phys. Rev. B* **2012**, 86, 235147.
- [56] D. Edwards, *Handbook of Optical Constants of Solids*, Academic Press, San Diego, CA **1985**, pp. 547–569.